Tunable interface strain coupling and its impact on the electronic transport and magnetic properties of $La_{0.5}Ca_{0.5}MnO_3/Pb(In_{1/2}Nb_{1/2})O_3$-$Pb(Mg_{1/3}Nb_{2/3})O_3$-$PbTiO_3$ multiferroic heterostructures

M. Zheng,[1] M. M. Yang,[1] Q. X. Zhu,[1] X. Y. Li,[1] G. Y. Gao,[2] R. K. Zheng,[1,*] Y. Wang,[3] X. M. Li,[1] X. Shi,[1] H. S. Luo,[1] and X. G. Li[2,4]

[1]*State Key Laboratory of High Performance Ceramics and Superfine Microstructure, Shanghai Institute of Ceramics, Chinese Academy of Sciences, Shanghai 200050, China*

[2]*Hefei National Laboratory for Physical Sciences at Microscale and Department of Physics, University of Science and Technology of China, Hefei 230026, China*

[3]*Department of Applied Physics, The Hong Kong Polytechnic University, Hong Kong, China*

[4]*Collaborative Innovation Center of Advanced Microstructures, Nanjing University, Nanjing, 210093, People's Republic of China*

(Received 22 September 2014; revised manuscript received 4 December 2014; published 22 December 2014)

A comprehensive understanding of strain coupling across heterointerfaces and its impact on physical properties of oxide heterostructures is important for elucidating the mechanisms of certain novel physical phenomena occurring at heterointerfaces, such as magnetoelectric coupling, tunneling electroresistance effects, and strain-driven exchange bias. Using the $La_{0.5}Ca_{0.5}MnO_3/Pb(In_{1/2}Nb_{1/2})O_3$-$Pb(Mg_{1/3}Nb_{2/3})O_3$-$PbTiO_3$ (PINT) multiferroic heterostructure as a model system, we systematically investigated the influences of interface strain coupling on the electronic transport and magnetic properties as well as the electronic phase separation of charge-ordered $La_{0.5}Ca_{0.5}MnO_3$ thin films through electric-field-induced ferroelectric domain switching. Upon the irreversible initial poling of the PMNT substrate, the induced in-plane compressive strain ($\varepsilon_{xx(\text{film})} = -0.045\%$) causes a decrease in T_{CO}($\Delta T_{CO} = 180$ K) and resistance [$(\Delta R/R)_{\text{strain}} \sim -99.4\%$], resulting in a gauge factor $(\Delta R/R)_{\text{strain}}/\varepsilon_{xx(\text{film})} \sim 220\,800\%$. Such a large strain-tunability of resistance is unprecedented and magnetic-field tunable. This, together with the strain-tunable magnetoresistance (*MR*) and magnetization of the films, demonstrates strong coupling between the strain and the magnetic field. Further analysis indicates that this coupling is essentially mediated by the electronic phase separation, whose relative strength could be monitored by measuring $(\Delta R/R)_{\text{strain}}$ against magnetic field and temperature. By combining 180° ferroelectric domain switching and x-ray diffraction and transport measurements, we identify that this electric-field modulation of the physical properties is strain-mediated but not interface charge-mediated. In addition, we observed that the non-180° ferroelastic domain switching-induced in-plane tensile strain ($\varepsilon_{xx(\text{film})} = 0.1\%$) induces a large increase in the resistance (up to ~87.4%) and T_{CO} and a drop in *MR*, signaling the stabilizing of the charge-ordered phase. Our findings provide further insight into the strain effect and essential physics of perovskite manganites, particularly the electronic phase separation.

DOI: 10.1103/PhysRevB.90.224420 PACS number(s): 75.85.+t, 77.55.Nv, 77.80.bn, 77.80.Jk

I. INTRODUCTION

Half-doped $La_{0.5}Ca_{0.5}MnO_3$ (LCMO) manganite situates at the phase boundary between the ferromagnetic metallic (FMM) ($x < 0.5$) phase and the charge-ordered antiferromagnetic insulating (CO/AFI) ($x > 0.5$) phase, and exhibits fascinating physical phenomena such as electronic phase separation and charge, spin, and orbital orderings [1,2]. Upon cooling, the LCMO first undergoes a paramagnetic to ferromagnetic (FM) phase transition around 225 K and then follows a first-order transition to the CO/AFI state around ~155 K [3]. Under application of a magnetic field, a portion of the CO/AFI phase would be converted to the FMM phase, resulting in a stronger electronic phase separation. In the past decade, the structural, electronic, and magnetic properties of LCMO bulk materials, either in the form of single crystals or polycrystalline, have been discussed at length in the literature. By contrast, the strain effects (i.e., the influences of strain imposed by substrates on physical properties) of LCMO films are much less known. Only very limited work concerning the strain effects of LCMO films has been reported [4–9]. It is noteworthy that Aydogdu *et al.* [4,5] reported that substrate-induced strain could change the ground state from CO/AFI to FMM for (111)-oriented LCMO films ($t = 145, 290$ nm) epitaxially grown on $SrTiO_3$ (111) substrates. These features are in contrast to those of (001)-oriented LCMO films, which are insulating ($dR/dT < 0$) down to the lowest temperature under zero magnetic field [6–8]. It should be noted that besides the substrate-induced strain, the oxygen content of $La_{0.5}Ca_{0.5}MnO_{3-y}$ has a tremendous impact on the volume fractions of the FMM and CO/AFI phases by modifying the Mn^{3+}/Mn^{4+} ratio, leading to drastic modification of the electronic transport and magnetic properties of the films [10–12]. Namely, oxygen deficiencies would push the doping level of $La_{0.5}Ca_{0.5}MnO_{3-y}$ towards the $x < 0.5$ FMM side, resulting in a FMM ground state and insulator-to-metal phase transition [13]. Therefore, it is highly important that all studied LCMO films should have the same and fixed oxygen content when one studies the strain effects of LCMO films. Yet, it is a highly challenging task to prepare a series of LCMO thin film samples with the same oxygen content. Fortunately, recent experimental studies on $La_{1-x}Sr_xCoO_3/Pb(Mg_{1/3}Nb_{2/3})O_3$-$PbTiO_3$ (PMNT) [14,15], $R_{1-x}A_xMnO_3$/PMNT (R = La, Pr; A =

*zrk@ustc.edu

Ca, Sr, Ba) [16–23], VO_2/PMNT [24], Fe_3O_4/PMNT [25], $CoFe_2O_4$/PMNT [26–28], $BiFeO_3/La_{0.7}Sr_{0.3}MnO_3$/PMNT [29,30], $La_{1-x}A_xMnO_3$(A = Ca, Sr)/$BaTiO_3$ [31–33], and $Fe_3O_4/BaTiO_3$ [34,35] heterostructures have demonstrated that the strain responses of electronic and magnetic properties can be *in situ* rigorously studied by epitaxially growing oxide thin films on ferroelectric (FE) substrates, which is an unprecedented approach that allows one to better understand the intrinsic coupling mechanisms between the lattice and the spin and charge degrees of freedom in complex oxide thin films, without introducing the effects of discrepancy in oxygen content from sample to sample.

On the other hand, it is still unclear whether or not the polarization reversal-induced interfacial electric charge could strongly modify the charge carrier density and subsequently the physical properties of complex oxide film/PMNT heterostructures. Since the doping level of the LCMO is at the phase boundary, it is anticipated that for LCMO/PMNT heterostructures, the polarization reversal-induced electric charge would push the doping level towards the CO/AFI side ($x > 0.5$) or the FMM side ($x < 0.5$) of the phase boundary. Unfortunately, the effects of polarization reversal on the physical properties of LCMO films are still missing and remain unaddressed for LCMO/PMNT heterostructures. There is no doubt that an in-depth understanding of polarization reversal-induced interfacial charge effects and a discrimination between the strain effect and the charge effect would help to understand the essential physics of manganites and the design of magnetoelectric electronic devices based on manganites, especially half-doped LCMO films. Moreover, certain important issues concerning the LCMO film still remain unclear, e.g., how the relative strength of electronic phase separation evolves with lattice strain, magnetic field, and temperature, and the mutual interaction between the lattice strain and the magnetic field.

Motivated by these unanswered questions, we systematically studied the electronic transport and magnetic properties as well as the electronic phase separation of LCMO films epitaxially grown on (001)-oriented $0.67Pb(Mg_{1/3}Nb_{2/3})O_3$-$0.33PbTiO_3$ (PMNT) and (111)-oriented $0.31Pb(In_{1/2}Nb_{1/2})O_3$-$0.35Pb(Mg_{1/3}Nb_{2/3})O_3$-$0.34PbTiO_3$ (PINT) single-crystal substrates. We *in situ* modified the strain state of LCMO films through FE poling along the [001] and [111] crystal directions, the converse piezoelectric effect, the ferroelastic effect, the 180° polarization reversal, and the electric-field-induced structural phase transition, and paid particular attention to the mutual interactions between the lattice strain and the magnetic field, the evolution of the strength of electronic phase separation with temperature, lattice strain, and magnetic field, the effects of 180° polarization reversal on transport properties, and the nonvolatile resistance switching of the LCMO film using the ferroelastic domain switching of the FE substrates.

II. EXPERIMENTAL DETAILS

The PMNT and PINT single-crystal boules with a size of $\Phi 50 \times 70\,mm^3$ were grown by a modified Bridgman technique at the Shanghai Institute of Ceramics. The crystal growth details were described in Ref. [36]. The as-grown PMNT and PINT crystal boules were cut into (001)- and (111)-oriented rectangular plates with a size of $10 \times 5 \times 0.5\,mm^3$ and carefully one-side polished to a root-mean-square roughness $R_q < 1\,nm$. The LCMO films were grown on the polished substrates by pulsed laser deposition. The laser energy density and repetition rate were $3\,J/cm^2$ and 5 Hz, respectively. Film deposition was carried out at a substrate temperature of 700 °C in 27 Pa oxygen pressure, followed by *in situ* annealing of the films in 1 atm O_2 for 30 min to reduce oxygen deficiencies and improve crystallinity. Then the films were cooled to room temperature at 5 °C/min.

Film thickness was measured by a FEI Magellan 400 scanning electron microscope operated in the backscattered electron (BSE) emission mode. The crystal structure and phase purity, as well as the epitaxial relationships of the films with respect to the FE substrates, were examined by means of θ-2θ linear scan, ϕ-scan, and reciprocal space maps using a high-resolution four-circle Bruker D8 Discover x-ray diffractometer equipped with 4-bounce Ge(220) monochromator and Cu$K_{\alpha 1}$ radiation ($\lambda = 1.5406$ Å). Cross-sectional transmission electron microscopy (TEM) specimens were prepared by face-to-face gluing of films and subsequent cutting into thin slices, followed by mechanical polishing, dimpling, and ion milling. The high-resolution structural observations of such prepared specimens were carried out on a Tecnai G2 F20 S-Twin transmission electron microscope. The surface morphology of LCMO films and the local FE responses of PINT substrates were characterized by means of atomic force microscopy (AFM) and piezoresponse force microscopy (PFM), respectively, using a Dimension V (Veeco) scanning probe microscope.

The electric-field-induced in-plane strain of the PINT substrate (i.e., $\delta\varepsilon_{xx(\mathrm{PINT})}$) was measured by a strain gauge that was attached onto the substrate surface with epoxy [see inset (b) of Fig. 11]. The FE poling, the converse piezoelectric effect, and the 180° FE and non-180° ferroelastic domain switching of FE substrates were achieved by applying a dc electric field across the substrates in the [001] or [111] direction using the LCMO film as the top electrode and the sputtered Au film (~100 nm) as the bottom electrode [Figs. 1(a) and 1(b)]. Four top Au electrodes were prepared on the surface of the LCMO films through a shadow mask using the magnetron sputtering method in order to form Ohmic contact for electronic transport measurements.

Magnetotransport and magnetic properties of the LCMO films were measured using a Physical Property Measurement System (PPMS-9, Quantum Design) and a superconducting quantum interference device (SQUID) magnetometer (MPMS XL-5, Quantum Design), respectively, with the direction of magnetic field applied parallel to the film plane. The longitudinal piezoelectric coefficient and the dielectric permittivity (ε_r) of PINT substrates were measured using a Berlincourt-type quasistatic d_{33} meter (ZJ-4AN, Institute of Acoustics, CAS) and an Agilent E4980 Precision LCR Meter, respectively. A Precision Multiferroic Analyzer (Radiant Technologies, Inc., USA) was employed to measure the polarization-electric field (P-E) hysteresis loop of the PMNT and PINT substrates at room temperature.

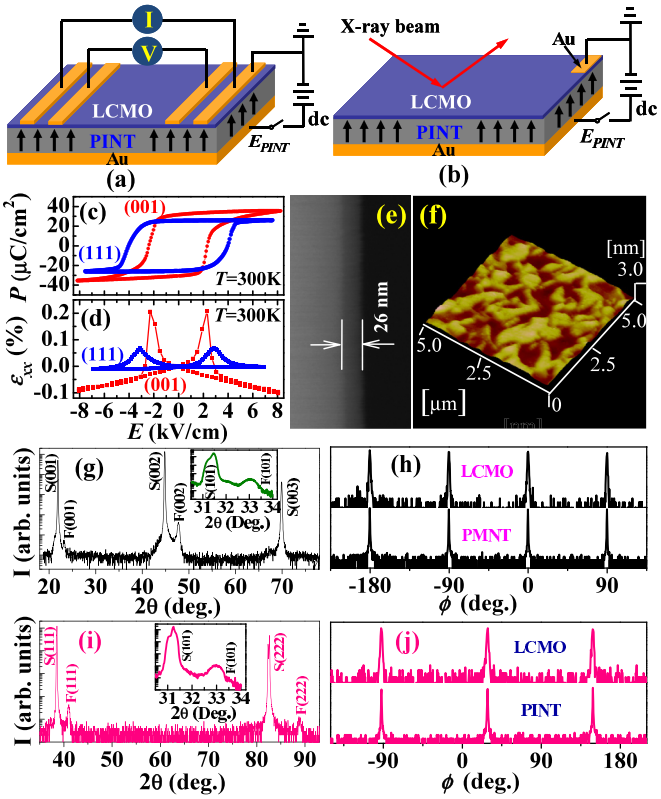

FIG. 1. (Color online) (a) and (b) Schematic of the experimental setups for *in situ* measurements of film resistance and strain. (c) and (d) Polarization and in-plane strain versus E for the PMNT(001) (red) and PINT(111) (blue) substrates. (e) and (f) Cross-sectional BSE image and surface morphology of a LCMO(111) film. (g) and (i) XRD θ-2θ scans of the LCMO films. "S" and "F" represent the substrates and films, respectively. (h) and (j) XRD ϕ scans taken on the (101) diffraction peaks of the films and substrates.

III. RESULTS AND DISCUSSION

A. Measurement setups, ferroelectric, piezoelectric, structural, and strain state of the LCMO/PMNT and LCMO/PINT structures

Figures 1(a) and 1(b) show a schematic diagram of the experimental setups for *in situ* measurements of the film resistance using the standard four-probe method and of the electric-field-induced out-of-plane strain of the film [$\delta\varepsilon_{zz(\mathrm{LCMO})}$] using x-ray diffraction (XRD) θ-2θ scans, respectively. For both setups, the FE substrates were poled along the thickness direction (i.e., along the [001] or [111] direction). Here, $\delta\varepsilon_{zz(\mathrm{LCMO})}$ is calculated using the equation

$$\delta\varepsilon_{zz(\mathrm{LCMO})} = [c_{\mathrm{LCMO}}(E) - c_{\mathrm{LCMO}}(0)]/c_{\mathrm{LCMO}}(0),$$

where $c_{\mathrm{LCMO}}(E)$ and $c_{\mathrm{LCMO}}(0)$ are the out-of-plane lattice constants of LCMO films when an electric field E or a zero electric field was applied across the FE substrates. Both the PMNT and PINT substrates exhibit symmetrical butterflylike strain-electric field loops [Fig. 1(d)] and quite good ferroelectricity at room temperature, as evidenced by the well-defined rectangular-shaped P-E hysteresis loops with remnant polarization $P_r \sim 32$ and 25 μC/cm^2 for the former and the latter [Fig. 1(c)], respectively. However, piezoelectric measurements using a Berlincourt-type quasistatic d_{33} meter showed that the longitudinal piezoelectric coefficient d_{33} of the PMNT substrate (~1800 pC/N) is much larger than that of the PINT substrate (~100 pC/N) because the chemical composition of the former is within the morphotropic phase boundary of the phase diagram, while the stated chemical composition of the latter is mainly a tetragonal phase whose d_{33} is much smaller than that of the rhombohedral phase [37]. The thickness of the LCMO films is ~26 nm, as illustrated by the cross-sectional BSE image shown in Fig. 1(e). All LCMO films show a rather smooth surface with $R_q \sim 1$ nm, as can be seen from the selected AFM image in Fig. 1(f).

Figures 1(g) and 1(i) display the XRD θ-2θ scan patterns of the LCMO films grown on the PMNT(001) and PINT(111) substrates, respectively. Only two sets of $(00l)$ $(l = 1, 2, 3)$ and (lll) $(l = 1, 2)$ diffraction peaks from the LCMO films and the PMNT and PINT substrates appear, suggesting that the LCMO films are of single phase and highly (001)- and (111)-oriented, respectively. XRD ϕ scans taken on the LCMO (101), PMNT (101), and PINT (101) reflections yield two sets of fourfold and trifold symmetrical diffraction peaks from the LCMO films [Figs. 1(h) and 1(j)], respectively, revealing the "cube-on-cube" epitaxial nature of the LCMO films on the FE substrates. For the LCMO(001) film, the out-of-plane lattice constant c, calculated from the out-of-plane θ-2θ scan data, is ~3.806 Å, which agrees with that (~3.805 Å) obtained from the reciprocal space map shown in Fig. S1(a) of the Supplemental Material [38]. The in-plane lattice constant a is ~3.858 Å, deduced from the off-axis θ-2θ scan data [inset of Fig. 1(g)] using the equation $a = 2\sqrt{(d_{101})^2 - (d_{002})^2}$, where d_{101} and d_{002} are the lattice spacings of the (101) and (002) planes [39], respectively, resulting in the tetragonality ratio $c/a = 0.986$. This means that the LCMO(001) film is subjected to an out-of-plane compressive ($\varepsilon_{zz(001)} \sim -0.7\%$) and in-plane tensile strain ($\varepsilon_{xx(001)} \sim 0.65\%$), in accordance with the fact that the lattice constants of the LCMO bulk material ($a \sim b \sim c \sim 3.833$ Å) are smaller than those of the PMNT substrate ($a \sim b \sim c \sim 4.02$ Å). Using the equation $\varepsilon_{zz} = -2\nu/(1-\nu)\varepsilon_{xx}$ [40,41], the Poisson's ratio ν of the LCMO film is calculated to be ~0.35, in agreement with typical values ranging from 0.3 to 0.5 for most materials, e.g., $\nu = 0.37$, 0.33, and 0.33 for $La_{0.7}Sr_{0.3}MnO_3$ [41], $LaCoO_3$ [42], and $BiFe_{0.95}Mn_{0.05}O_3$ [29] films, respectively. Note that for the LCMO(111) film on the PINT, the calculated lattice spacing d for the family of (111) planes (~2.199 Å) is also smaller than that of the LCMO(111) bulk material (~2.213 Å), implying that the LCMO(111) film is also subjected to an out-of-plane compressive ($\varepsilon_{zz(111)} \sim -0.68\%$) and in-plane tensile ($\varepsilon_{xx(111)} \sim 0.63\%$) strain.

Transmission electron microscopy was employed to further examine the epitaxial relationship of the LCMO/PINT(111) heterostructure. The image in the inset of Fig. 2(a) shows that the thickness of the LCMO(111) film is ~26 nm, being consistent with the BSE image in Fig. 1(e). The high-resolution TEM image in Fig. 2(a) reveals coherent film/substrate interface and in-plane epitaxial relationships of LCMO(001)//PINT(001) and LCMO(110)//PINT(110). The image also displays clear lattice fringes with lattice spacings of 0.386 nm for the family of (001) planes and 0.27 nm for the family of (110) planes. The epitaxial arrangement of the LCMO(111) film on the

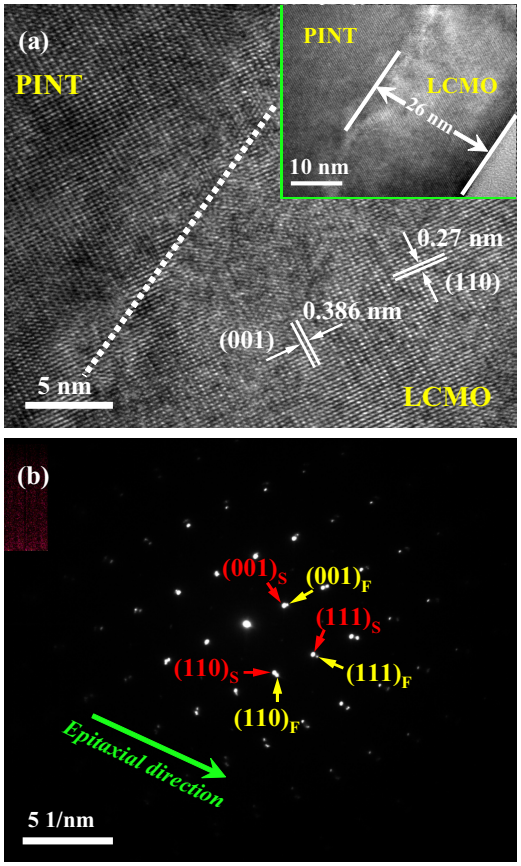

FIG. 2. (Color online) (a) High-resolution TEM image for the LCMO/PINT(111) heterostructure (inset) and an enlarged interface region. (b) SAED pattern of the LCMO/PINT interface. Red and yellow arrows indicate diffraction patterns from the PINT and the LCMO, respectively.

PINT(111) substrate was further confirmed by the selected area electron diffraction (SAED) pattern [Fig. 2(b)] taken from a selected area containing both the PINT substrate and the LCMO film. Due to the difference in the lattice constants between the PINT and the LCMO, two appreciable sets of diffraction patterns were identified, corresponding to the PINT (strong spots) and LCMO (weak spots) lattice, respectively.

B. Effects of FE poling on the strain state, electronic transport, and magnetic properties of the LCMO films

In order to explore the FE poling-induced dynamical strain on the electronic transport properties, we plotted the relative change of the resistance ($\Delta R/R$) as a function of the electric field applied across the PMNT and PINT substrates in Fig. 3. Whether the LCMO films are (001)- or (111)-oriented, the resistance shows a nonlinear abrupt drop near E_C (~2.5 kV/cm) of the PMNT and PINT substrates. XRD θ-2θ scan measurements on the LCMO/PMNT(001) and LCMO/PINT(111) structures show that the reflections from the LCMO films and FE substrates both shift to lower 2θ angles. Selected XRD θ-2θ scan patterns in the vicinity of PINT(111) and LCMO(111) for the LCMO/PINT(111) structure are shown in Fig. S2 of the Supplemental Material [38], where a noticeable shift in the reflections towards lower

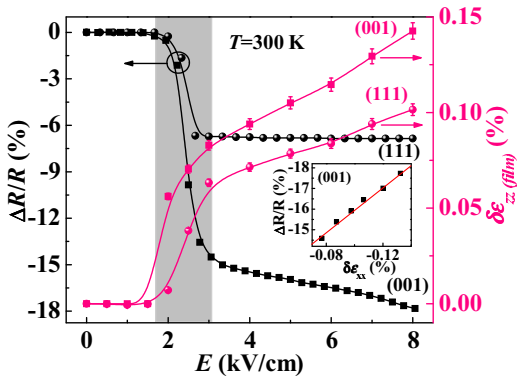

FIG. 3. (Color online) $\Delta R/R$ and electric-field-induced out-of-plane strain $\delta\varepsilon_{zz(\text{film})}$ of the LCMO films as a function of E. Inset: $\Delta R/R$ versus the electric-field-induced in-plane strain $\delta\varepsilon_{xx(\text{film})}$ for the LCMO(001) film.

2θ angle can be appreciated between $E = 2$ and 4 kV/cm. Using these XRD data, we calculated and plotted the electric-field-induced out-of-plane strain $\delta\varepsilon_{zz(\text{LCMO})}$ of the LCMO films in Fig. 3. $\delta\varepsilon_{zz(\text{LCMO})}$ exhibits a nonlinear abrupt increase near E_C (~2.5 kV/cm) and increases linearly for $E > 4$ kV/cm. It can be appreciated that $\Delta R/R$ follows the change of $\delta\varepsilon_{zz(\text{LCMO})}$ effectively during the poling, demonstrating intimate correlation between the electronic transport properties and the strain state of the film. For $E = 8$ kV/cm, the electric-field-induced $\delta\varepsilon_{zz(\text{LCMO})}$ for the LCMO(001) film is ~0.143%. This value is consistent with $\delta\varepsilon_{zz(\text{LCMO})} \sim 0.164\%$ under $E =$ 10 kV/cm, obtained from the reciprocal space maps shown in Figs. S1(a) and S1(b) of the Supplemental Material [38]. Using the Poisson relation $\delta\varepsilon_{zz(\text{film})} = -2\nu/(1-\nu)\delta\varepsilon_{xx(\text{film})}$ and $\nu = 0.35$ for the film, the electric-field-induced in-plane strain $\delta\varepsilon_{xx(\text{film})}$ for the LCMO(001) film is estimated to be ~−0.13% at $E = 8$ kV/cm. Accordingly, the room temperature gauge factor β, $\beta = (\Delta R/R)_{\text{film}}/\varepsilon_{xx(\text{film})}$, is calculated to be ~137 at $E = 8$ kV/cm for the LCMO(001) film, which is comparable to the value (~150) for the $La_{0.7}Sr_{0.3}MnO_3/0.72PbMg_{1/3}Nb_{2/3}O_3$-$0.28PbTiO_3$ structure [43], demonstrating the strong electron-lattice coupling in the LCMO(001) film. Note that for the LCMO(001) film, $\Delta R/R$ decreases linearly with increasing E from ~ 3 to 8 kV/cm, which is due to the linear converse piezoelectric effect and is further corroborated by the linear dependence of $\Delta R/R$ on the induced in-plane strain of the film (see the inset of Fig. 3). For the LCMO(111) film, $\Delta R/R$ for $E \geqslant 3$ kV/cm also has a linear response to the applied electric field, with the slope [i.e., $d(\Delta R/R)/dE$] much smaller than that of the LCMO(001) film. This is in accordance with the fact that d_{33} of the PINT(111) (~100 pC/N) is much smaller than that of the PMNT(001) (~1800 pC/N). Note that the effects of the converse piezoelectric effect on the transport properties of the LCMO/PIN(111) structure will be further discussed later. We note that the poling-induced remnant out-of-plane strain in the LCMO(001) and LCMO(111) films is estimated to be ~0.048% and 0.04%, respectively, by extrapolating the linear part of the $\delta\varepsilon_{zz(\text{LCMO})}$ versus E curves to zero electric field (see Fig. S3 of the Supplemental Material [38]). Again, using the equation $\delta\varepsilon_{zz(\text{film})} = -2\nu/(1-\nu)\delta\varepsilon_{xx(\text{film})}$ and $\nu = 0.35$,

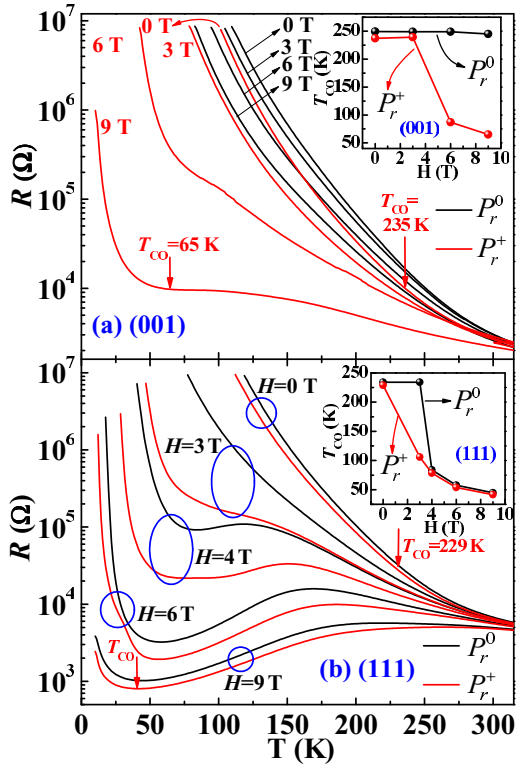

FIG. 4. (Color online) Temperature dependence of the resistance for the LCMO films in the magnetic fields as stated when the PMNT(001) (a) and PINT(111) (b) substrates were in the P_r^0 and P_r^+ states, respectively. Insets show the corresponding T_{CO} versus H curves for the P_r^0 and P_r^+ states, respectively.

the poling-induced remnant in-plane strain in the LCMO(001) and LCMO(111) films is calculated to be $\sim -0.045\%$ and -0.037%, respectively. Such a small poling-induced in-plane lattice compression has tremendous impact on the electronic transport properties and will be discussed in the following sections.

Figures 4(a) and 4(b) show the temperature dependence of the resistance at different magnetic fields for the LCMO/PMNT(001) and LCMO/PINT(111) heterostructures, respectively, where the PMNT(001) and PINT(111) substrates were in the unpoled P_r^0 and positively poled P_r^+ states, respectively. Here, P_r^+ is defined as the polarization direction points to the LCMO film. For the P_r^0 state and $H = 0$ T, the resistance of the LCMO(111) film increases with decreasing temperature and undergoes a charge-ordering phase transition at $T_{CO} \sim 229$ K. Here, T_{CO} was derived from the $d(\ln R)/d(T^{-1}) - T$ curve (not shown here). With increasing H to 4 T, a significant part of the CO/AFI phase was converted to the FMM phase, as reflected by the magnetic-field-induced large decrease in the resistance and suppression of T_{CO} from 229 K for $H = 0$ T to 84 K for $H = 4$ T. As H increases further, both the resistance and T_{CO} were further reduced, meaning that the CO/AFI phase was further converted to the FMM phase. Note that after the unpoled PINT(111) substrate had been fully poled along the [111] direction at room temperature by applying a dc electric field of 8 kV/cm to the LCMO/PINT(111) structure, the CO/AFI phase was partly melted and converted to the FMM phase by the poling-induced strain, as manifested by the poling-induced decrease in the resistance over the whole temperature range for a fixed magnetic field. Particularly, for $H = 4$ T, the poling-induced strain reduces the resistance remarkably. In addition, the poling-induced strain results in a large change in T_{CO}. As shown in the inset of Fig. 4(b), ΔT_{CO} [$\Delta T_{CO} = T_{CO}(P_r^0) - T_{CO}(P_r^+)$] for the LCMO(111) film has a maximum value of ~ 128 K at $H = 3$ T, indicating that T_{CO} is most sensitive to the poling-induced strain at $H = 3$ T, whereas for $H > 3$ T, the poling-induced strain has minor effect on T_{CO}. The strong dependence of poling-induced ΔT_{CO} on H reflects that the magnetic field could strongly influence the strain effects. For the LCMO/PINT(001) structure, whether with the application of a magnetic field or substrate poling, the CO/AFI phase at low temperature (e.g., 10 K) is still stable, as reflected by the insulating nature of the resistance at the P_r^+ state for $H = 9$ T. Again, the magnetic field has a strong impact on the strain effect for the LCMO/PMNT(001) structure [Fig. 4(a)], where we observed that the CO/AFI phase is extremely sensitive to the poling-induced strain, which is manifested by the reduction of the resistance by approximately more than three orders of magnitude near $T = 65$ K. As shown in the inset of Fig. 4(a), the poling-strain-induced ΔT_{CO} also strongly depends on the magnetic field for $H > 3$ T and reaches ~ 180 K for $H = 9$ T. This value ($\sim$180 K) is much larger than that for the LCMO(111) film ($\sim$128 K), which could be due to the larger induced strain in the LCMO(001) film (see Fig. 3) and the stronger electronic phase separation in the LCMO(001) film, which will be discussed in detail later. All these electronic transport data strongly demonstrate that the poling-induced strain effect is strongly influenced by the magnetic field, which could modify the volume fractions of the coexisting CO/AFI and FMM phases. We recall that previous magnetotransport results on the $La_{0.7}Ca_{0.15}Sr_{0.15}MnO_3$/PMNT structures have demonstrated that the maximum poling-induced strain effects appear near the paramagnetic-to-FM phase transition temperature T_C, where the strength of the electronic phase separation shows the maximum [44]. It is thus anticipated that the magnetic-field-tunable strain effects are closely correlated with the electronic phase separation.

To quantify the response of the resistance to the poling-induced strain and gain greater insight into the electronic phase separation for the LCMO(001) and LCMO(111) films, we plotted the strain-tunability of resistance, $(\Delta R/R)_{strain}$, as a function of temperature in Figs. 5(a) and 5(b), respectively. Here, $(\Delta R/R)_{strain}$ is defined as $(\Delta R/R)_{strain} = [R(P_r^0) - R(P_r^+)]/R(P_r^0)$. For the LCMO(111) film, $(\Delta R/R)_{strain}$ at $H = 0$ T increases continuously upon decreasing temperature, implying increasing sensitivity of the CO/AFI phase to the strain at low temperatures. We emphasize that $(\Delta R/R)_{strain}$ is strongly dependent on the magnetic field, especially at low temperatures. For example, $(\Delta R/R)_{strain}$ at $T = 150$ K is enhanced from 29.7% for $H = 0$ T to 59.5% for $H = 4$ T, and then it decreases with increasing H from 4 to 9 T. $(\Delta R/R)_{strain}$ at $T = 77$ K is dramatically suppressed from 97.3% for $H = 3$ T to 20.5% for $H = 9$ T, a reduction of approximately 78.9%. Such considerable magnetic-field-tunable $(\Delta R/R)_{strain}$ has not yet been observed for $R_{1-x}A_xMnO_3$/PMNT ($R =$

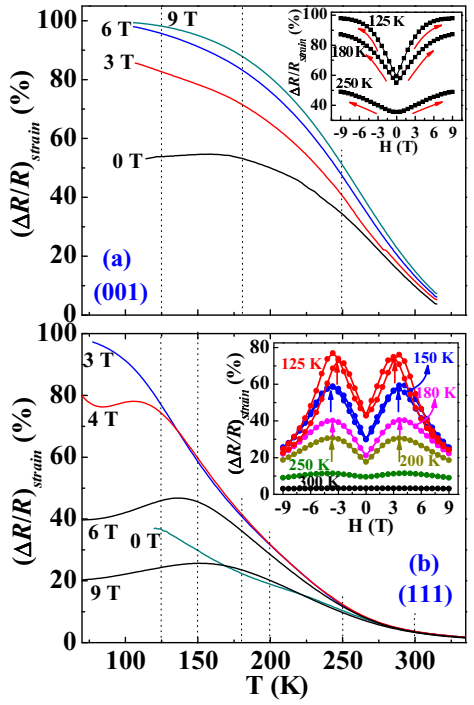

FIG. 5. (Color online) Temperature dependence of $(\Delta R/R)_{\text{strain}}$ in the magnetic fields as stated for the LCMO(001) (a) and LCMO(111) (b) films, respectively. Insets show corresponding $(\Delta R/R)_{\text{strain}}$ versus H curves for the LCMO films at the temperatures stated.

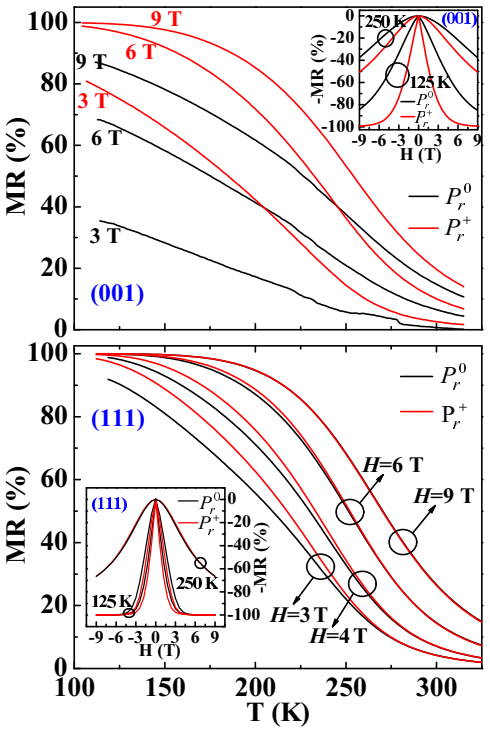

FIG. 6. (Color online) Temperature dependence of MR for the LCMO films in the magnetic fields as stated when the PMNT(001) (a) and PINT(111) (b) substrates were in the P_r^0 and P_r^+ states, respectively. Insets show corresponding MR versus H curves for the P_r^0 and P_r^+ states at the temperatures stated.

La, Pr, A = Ca, Sr) systems. Note that the evolution of $(\Delta R/R)_{\text{strain}}$ with H for the LCMO(111) film is better seen in the inset of Fig. 5(b), where we plot $(\Delta R/R)_{\text{strain}}$ as a function of H. At a fixed temperature (e.g., $T = 125$ K), $(\Delta R/R)_{\text{strain}}$ has a maximum value of 74.8% at $H = 3$ T (red filled symbol), indicating that the strength of the electronic phase separation is the strongest at $H = 3$ T for $T = 125$ K, where the CO/AFI phase and the FMM phase reach a subtle balance and the energy difference between them is minimum. A small external perturbation (e.g., poling-induced strain) could easily convert the CO/AFI phase to the FMM phase, causing a large decrease in the resistance of up to 74.8%. For $T = 180$ K, the strongest electronic phase separation appears at $H = 3.6$ T, since $(\Delta R/R)_{\text{strain}}$ shows the maximum value (~40.5%) there. For high temperatures (e.g., $T =$ 250 and 300 K), $(\Delta R/R)_{\text{strain}}$ under any H is much smaller than that at low temperatures (e.g., $T = 125$ and 150 K), and moreover $(\Delta R/R)_{\text{strain}}$ is weakly dependent on the magnetic field. This is consistent with the fact that the electronic phase separation in the high-temperature paramagnetic state is very weak. In contrast, for the LCMO(001) film, the maximum electronic phase separation tendency does not appear, even for $H = 9$ T, since there is no peak value in the isothermal $(\Delta R/R)_{\text{strain}}$ versus H curves shown in the inset of Fig. 5(a), where $(\Delta R/R)_{\text{strain}}$ increases monotonously with increasing H and reaches 99.4%. This could be attributed to the relatively large initial in-plane tensile strain that stabilizes the CO/AFI phase, and thus the CO/AFI phase dominates over the FMM phase in the LCMO(001) film, even with the application of a sufficient large magnetic field (e.g., $H = 9$ T). Consequently, the relative strength of the electronic phase separation was enhanced continuously by H, leading to the magnetic-field-induced enhancement of $(\Delta R/R)_{\text{strain}}$ throughout the entire temperature range [see Fig. 5(a)]. The data discussed above clearly demonstrate that the magnetically tunable strain effect is closely related to electronic phase separation, whose strength can be monitored by measuring $(\Delta R/R)_{\text{strain}}$ under the application of magnetic fields.

The mutual interactions between the magnetic field and the poling-induced strain are manifested not only by the magnetically tunable strain effect, but also by the strain-tunable MR effect. The latter effect is shown in Fig. 6(a), where the MR of the LCMO(001) film is greatly enhanced over the whole temperature range after poling. The relative change in MR, $\Delta MR/MR = [MR(P_r^+) - MR(P_r^0)]/MR(P_r^0)$, reaches 120% at $T = 114$ K for $H =$ 3 T, which is quite superior to earlier reports on manganite films/PMNT systems [44]. Such significantly enhanced MR is also seen in the inset of Fig. 6(a), where MR was plotted against H for the P_r^0 and P_r^+ states, respectively, and can also be understood in terms of the electronic phase separation, the strength of which is enhanced by the poling-strain-induced conversion of the CO/AFI phase to the FMM phase. Similar trends can be identified for the LCMO(111) film shown in Fig. 6(b). However, one can find that with increasing H, the impact of the poling-induced strain on MR is gradually suppressed. Especially for $H = 9$ T, there is no visible change in MR upon substrate poling. We recall that transport data in

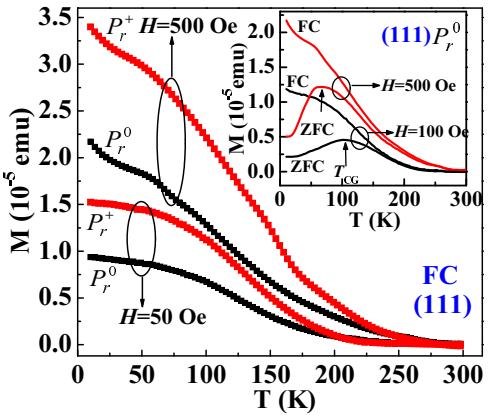

FIG. 7. (Color online) Temperature dependence of FC magnetization for the LCMO(111) film when the PINT substrate was in the P_r^0 and P_r^+ state, respectively. Inset: temperature dependence of ZFC and FC magnetization for the LCMO(111) film when the PINT substrate was in the unpoled P_r^0 state.

Fig. 4(b) have shown that with the application of a sufficiently large magnetic field (e.g., $H = 9\,T$), the CO/AFI phase was almost completely converted to the FMM phase, as reflected by the $MR \sim 99.98\%$ at $T = 112$ K. Thus, the LCMO(111) film is mainly composed of the FMM phase at $H = 9$ T. Under such circumstance, the poling-induced strain is unable to convert the remaining CO/AFI patches to the FMM matrix, since there is indeed almost no CO/AFI phase under $H = 9$ T. These results demonstrate that the strain and the magnetic field strongly couple with each other and are deeply mediated by the electronic phase separation.

Associated with these changes in the transport properties, the magnetic properties of the LCMO(111) film were also significantly modified by the poling-induced strain. Similar to the findings reported previously for the LCMO film [4,12], a pronounced magnetic irreversibility between the zero-field-cooled (ZFC) and field-cooled (FC) magnetization versus temperature curves is observed for $H = 100$ and 500 Oe (the inset of Fig. 7), respectively, implying a portion of FMM patches was imbedded in the CO/AFI matrix. Figure 7 displays the temperature dependence of FC magnetization of the LCMO(111) film when the PINT substrate was in the P_r^0 and P_r^+ states, respectively. Upon poling of the PINT, a remarkable increase in the in-plane magnetization was observed at low temperatures. The magnetization at $T = 10$ K is enhanced by 62.6% and 56.5% for $H = 50$ and 500 Oe, respectively. This poling-strain-induced enhancement of the ferromagnetism is further collaborated by the magnetic hysteresis loops measured at various fixed temperature for the P_r^0 and P_r^+ states, as shown in Fig. 8, where a distinct increase in the remanent magnetization can be found upon poling. Such strain-mediated electric-field control of ferromagnetism is microscopically different from that observed in the $La_{0.8}Sr_{0.2}MnO_3/PbZr_{0.2}Ti_{0.8}O_3$ heterostructure, where the interfacial charge mediates the electric-field control of ferromagnetism [45]. Note that these magnetic data are consistent with the electronic transport results [Fig. 4(b)] and further support our earlier discussions that the poling-induced strain modifies the electronic phase separation by converting the CO/AFI phase to the FMM phase.

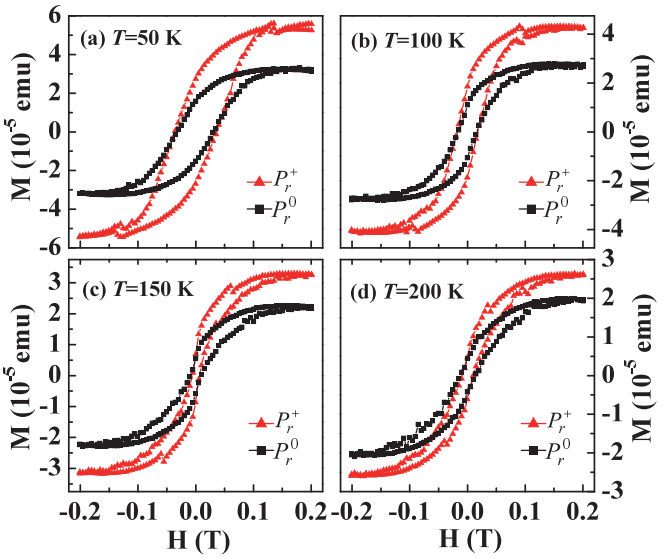

FIG. 8. (Color online) Magnetic hysteresis loops of the LCMO(111) film when the PINT substrate was in the P_r^0 and P_r^+ states at the temperatures stated.

C. Effects of the converse piezoelectric effect and the electric-field-induced structural phase transition on the transport properties of the LCMO films

In order to further understand the interactions between the strain and the magnetic field, we imposed linear in-plane compressive strain to the LCMO(111) film using the converse piezoelectric effect of the PINT(111) substrate and measured the relative resistance change $(\Delta R/R)_{\text{strain}}$ of the film as a function of the positive electric field E applied to the positively poled PINT(111) substrate at several fixed temperatures and magnetic fields. Selected $(\Delta R/R)_{\text{strain}}$ versus E curves at $H = 0$, 4.5, and 9 T for $T = 125$ and 150 K are presented in Fig. 9. The resistance decreases linearly with increasing E for $H = 0$, 4.5, and 9 T due to the converse-piezoelectric-effect-induced linear compression of the in-plane lattice of the film [21]. We note that the application of a magnetic field enhances the converse-piezoelectric-effect-induced strain effect and thus brings stronger strain-tunability of resistance.

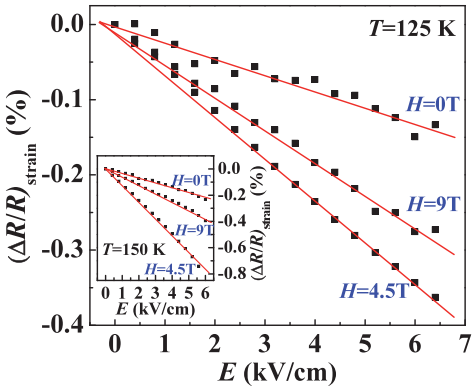

FIG. 9. (Color online) $(\Delta R/R)_{\text{strain}}$ of the LCMO(111) film as a function of positive E applied to the positively poled PINT(111) substrate under $H = 0$, 4.5, and 9 T at $T = 125$ and 150 K (inset).

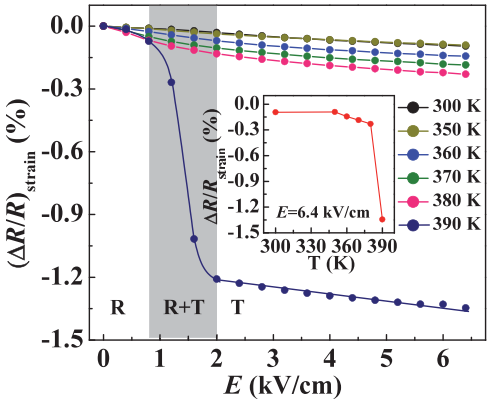

FIG. 10. (Color online) $(\Delta R/R)_{\text{strain}}$ of the LCMO(111) film as a function of positive E applied to the positively poled PINT(111) substrate at the temperatures stated. Inset: $(\Delta R/R)_{\text{strain}}$ at $E = 6.4\,\text{kV/cm}$ as a function of temperature.

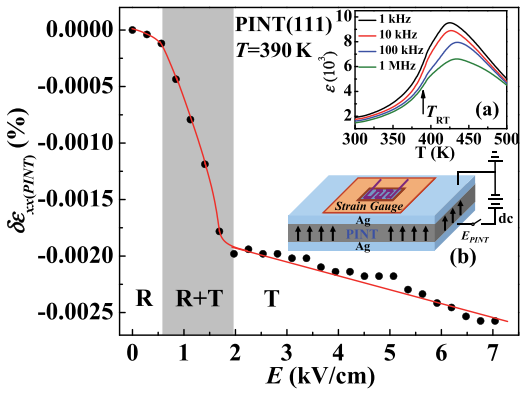

FIG. 11. (Color online) Electric-field-induced in-plane strain $\delta\varepsilon_{xx(\text{PINT})}$ as a function of positive E applied to the positively poled PINT substrate at $T = 390\,\text{K}$. Inset (a): temperature dependence of the dielectric permittivity of the PINT substrate. Inset (b): schematic of the experimental setups for measurements of electric-field-induced in-plane strain of the PINT substrate.

For $T = 125\,\text{K}$, the application of $H = 4.5\,\text{T}$ enhances $(\Delta R/R)_{\text{strain}}$ by ~170% at $E = 6.4\,\text{kV/cm}$. However, the application of a high field of $H = 9\,\text{T}$ reduces $(\Delta R/R)_{\text{strain}}$ by ~25% at $E = 6.4\,\text{kV/cm}$ when compared with that at $H = 4.5\,\text{T}$. These magnetically tunable $(\Delta R/R)_{\text{strain}}$ values again demonstrate strong coupling between the piezoelectric strain and the magnetic field and can be explained by taking account of the electronic phase separation in the LCMO(111) film. Specifically, at $T = 125\,\text{K}$, the application of a magnetic field with appropriate strength (e.g., $H = 4.5\,\text{T}$) would convert a portion of the CO/AFI phase to the FMM phase, resulting in a stronger electronic phase separation. Consequently, the converse-piezoelectric-effect-induced strain results in a larger $(\Delta R/R)_{\text{strain}}$. However, if a high field of $H = 9\,\text{T}$ was applied, almost all of the CO/AFI phase was converted to the FMM phase. The strength of the electronic phase separation is suppressed, resulting in the decrease of $(\Delta R/R)_{\text{strain}}$.

At higher fixed temperatures ($300\,\text{K} \leqslant T \leqslant 380\,\text{K}$), the resistance of the LCMO(111) film is also approximately linear dependent on E (Fig. 10), signaling the piezoelectric nature of the induced strain in the PINT(111) substrate at high temperatures. What is unexpected is that a nonlinear sharp drop in the resistance occurs near $E = 1.5\,\text{kV/cm}$ and ends at $E = 2\,\text{kV/cm}$ for $T = 390\,\text{K}$. For $E > 2\,\text{kV/cm}$, $(\Delta R/R)_{\text{strain}}$ shows linear dependence on E. $(\Delta R/R)_{\text{strain}}$ at $E = 6.4\,\text{kV/cm}$ is plotted against temperature in the inset of Fig. 10, where one can find that $(\Delta R/R)_{\text{strain}}$ is influenced by the variation of temperature, particularly near $T = 390\,\text{K}$. We remind the reader that previous dielectric measurements revealed that the PINT single crystal undergoes a spontaneous rhombohedral-to-tetragonal structural phase transition near $T \sim 390\,\text{K}$ [37,46]. Our dielectric measurements on the PINT substrate also showed that there is a small dielectric anomaly near $T \sim 390\,\text{K}$ [inset (a) of Fig. 11]. It is thus anticipated that the anomaly in $(\Delta R/R)_{\text{strain}}$ near $T = 390\,\text{K}$ is probably associated with the electric-field-induced structural instabilities. To clarify this point, we measured the electric-field-induced in-plane strain of the PINT substrate at $T = 390\,\text{K}$ using the experimental setup shown in the inset (b) of Fig. 11 and show the results in Fig. 11. Indeed, the electric field induces an appreciable in-plane compressive strain ($\delta\varepsilon_{xx(\text{PINT})}$) in the PINT substrate near $E = 1.25\,\text{kV/cm}$. Such electric-field-induced nonlinear change in $\delta\varepsilon_{xx(\text{PINT})}$ also ends at $E = 2\,\text{kV/cm}$, in agreement with the evolution of $(\Delta R/R)_{\text{strain}}$ with E. For $E > 2\,\text{kV/cm}$, $\delta\varepsilon_{xx(\text{PINT})}$ decreases approximately linearly with increasing E. The much weaker piezoelectric strain response above $E = 2\,\text{kV/cm}$ hints that the high-field phase is the tetragonal one [47]. Comparing the $(\Delta R/R)_{\text{strain}}$ versus E curve with the $\delta\varepsilon_{xx(\text{PINT})}$ versus E one, it is concluded that the electric-field-induced sharp drop in $(\Delta R/R)_{\text{strain}}$ at $T = 390\,\text{K}$ microscopically originates from the electric-field-induced rhombohedral-to-tetragonal structural phase transition of the PINT substrate. Note that similar electric-field-induced structural phase transitions have been observed in PMNT single crystals at high temperatures [47,48].

D. Effects of polarization reversal on the transport properties of the LCMO films

To further understand the role played by the strain and interfacial electric charge during the polarization reversal, we recorded the resistance change of the LCMO(111) film by sweeping the electric field, which was applied across the positively poled PINT(111) substrate, from 0 to $-7\,\text{kV/cm}$ and then back to 0 kV/cm. As illustrated in the inset of Fig. 12(a), with the increase of the negative reverse electric field E, the resistance of the film shows a considerable increase (~7.3%) near E_C(~3 kV/cm) of the PINT, where non-180° polarization direction reorientation occurs [49]. With further increase in the reverse $E\,(E > |-E_C|)$, the polarization direction undergoes another non-180° reorientation [49], accompanied by a sharp drop in the resistance. This two-stage polarization reorientation process results in a 180° polarization switching for all domains, i.e., the polarization points to the bottom Au electrode (denoted by P_r^-). Since the FE domain has a strong impact on the strain state, and electronic and magnetic properties of FM/FE heterostructures [50–52], we thus measured the PFM image of the PINT substrate before

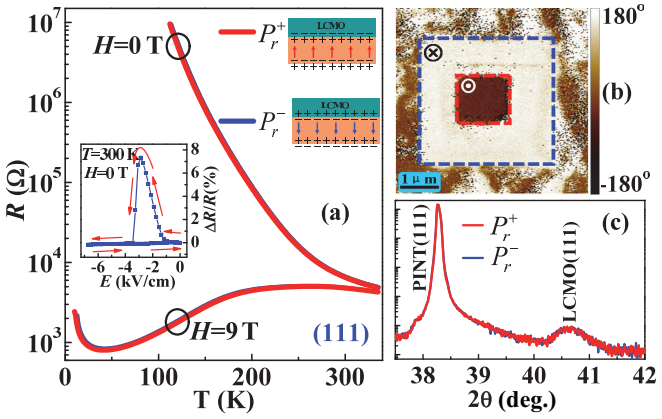

FIG. 12. (Color online) (a) Temperature dependence of resistance for the LCMO(111) film at $H = 0$ and 9 T when the PINT(111) substrate was in the P_r^+ and P_r^- states, respectively. Insets in (a): $\Delta R/R$ of the film as a function of negative E applied to the positively poled PINT substrate (lower panel) and schematic of the polarization switching-induced accumulation or depletion of charge carriers of the film. (b) PFM image of the PINT substrate. (c) XRD θ-2θ scans of the LCMO/PINT(111) heterostructure when the PINT substrate was in the P_r^+ and P_r^- states, respectively.

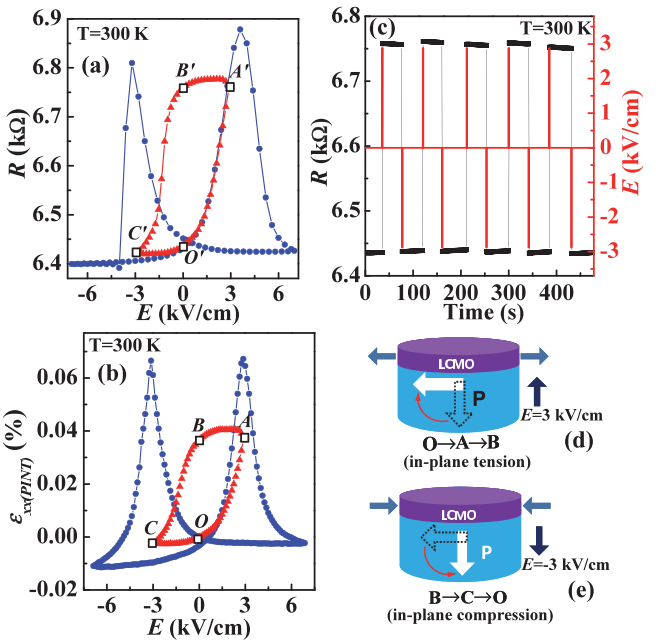

FIG. 13. (Color online) Electric-field-induced relative resistance change for the LCMO(111) film (a) and in-plane strain of the PINT substrate (b) as a function of bipolar and unipolar E applied across the PINT at $T = 300$ K. (c) Nonvolatile resistance switching of the LCMO(111) film by a pulse electric field at $T = 300$ K. (d) and (e) Schematic diagrams for the ferroelastic strain effect at $T = 300$ K.

and after 180° domain switching and showed the results in Fig. 12(b), where a region of the PINT was electrically switched to create a "box-in-box" architecture. Specifically, a $3.6 \times 3.6\ \mu m^2$ region was poled by applying a voltage of +8 V on the tip. Consequently, both FE domain switching (180°) and ferroelastic domain switching (71° and 109°) occur, and all the polarization vectors point downward within the area of the blue box. Subsequently, a smaller $1.3 \times 1.3\ \mu m^2$ region inside of the blue box was reversely poled by applying a poling voltage of −8 V. As a result, all of the polarization vectors point upward within the area of the red box. Sharp contrast appears in the out-of-plane direction, demonstrating that the PINT was fully poled to the P_r^+ or P_r^- state. After the PINT had been fully poled to the P_r^- state, the resistance of the film increased gently and linearly with decreasing E from −7 to 0 kV/cm, in agreement with the weak piezoelectricity ($d_{33} \sim 100$ pC/N) of the PINT(111) substrate. Due to the 180° polarization switching, no remnant strain was induced in the PINT substrate between the P_r^+ and the P_r^- state, which is revealed by the same peak position of the PINT(111) reflections for the two polarization states [Fig. 12(c)]. Accordingly, the strain state of the LCMO film was not modified after the polarization reversal. One can thus expect that the 180° polarization switching has no influence on the transport properties of the LCMO(111) film in light of strain effect. Indeed, whether the LCMO film was at $H = 0$ or 9 T, the resistance for the P_r^+ state is similar to that for the P_r^- state over the entire temperature range [Fig. 12(a)]. However, we recall that the 180° polarization-switching–induced electric charge at the surface of the FE substrate would be screened by an equal number of charge carriers of opposite sign in the film, resulting in electron accumulation or hole depletion in the LCMO film. Consequently, the resistance for the P_r^+ state should be larger than that for the P_r^- state if the polarization-switching-induced electric charge at the interface plays an important role and contributes to the electronic transport [53,54]. However, no such change in the resistance was observed upon the 180° polarization switching. From this reasoning, the FE field effect is believed to very weak in the heterostructure and has almost no influence on the properties of the LCMO film, demonstrating the strain-induced, not polarity-induced, nature of the resistance change.

E. Effects of ferroelastic domain switching on the resistance of the films

Using the ferroelastic domain switching of the PINT substrate, we further studied the strain effect in the LCMO/PINT(111) heterostructure by conducting reversible resistance switching of the LCMO film. In Fig. 13(a), we show the resistance of the film as a function of bipolar electric field applied across the PINT at $T = 300$ K. It can be found that the resistance response to the bipolar electric field E [$E > E_{C(\mathrm{PINT})}$] exhibits a typical approximately symmetrical butterflylike shape (blue). However, upon cycling the electric field with $E < E_{C(\mathrm{PINT})}$, a hysteretic looplike resistance versus E curve was observed, a result similar to that observed in the VO_2/PMNT [24] and Fe_3O_4/PMNT [25] heterostructures. In-plane strain measurements using a strain gauge demonstrate that 180° FE domain switching occurs when a bipolar E [$E > E_{C(\mathrm{PINT})}$] was applied to the PINT substrate. However, if a unipolar E[$E < E_{C(\mathrm{PINT})}$] was applied to the PINT substrate, non-180° domain switching was mainly induced, resulting in a hysteretic looplike strain versus E curve (red). With the application of either a bipolar or a unipolar E, the in-plane strain $\varepsilon_{xx(\mathrm{PINT})}$ versus E curves of the PINT

[Fig. 13(b)] show similar patterns as those of resistance versus E curves, which clearly demonstrate the strain-induced nature of the resistance change. It has been demonstrated by Wu *et al.* [49,55] that the FE domains have a metastable state during the polarization reversal in the vicinity of the coercive field. Therefore, this ferroelastic control of nonvolatile resistance switching can be qualitatively explained using the schematic diagrams shown in Figs. 13(d) and 13(e). When applying $E = +3\,\mathrm{kV/cm}$ [close to but lower than $E_{C(\mathrm{PINT})}$] to the negatively poled PINT substrate, a portion of the FE domain rotates from the downward direction towards the in-plane direction and thus induces an in-plane tensile strain, corresponding to the change of the strain state from ***O*** to ***A*** in Fig. 13(b). Once the $E = +3\,\mathrm{kV/cm}$ is turned off, the in-plane strain remains largely unchanged due to the stability of the remnant in-plane polarization of the PINT. This is directly reflected by the evolution of the strain state from ***A*** to ***B*** but not to ***O*** [Fig. 13 (b)]. Accordingly, the resistance of the film changes from ***O′*** to ***A′*** then to ***B′***. Afterwards, the in-plane polarization was switched back to the downward direction (from ***B*** to ***C***) with the application of $E = -3\,\mathrm{kV/cm}$ [Fig. 13(e)], releasing the previously induced remnant in-plane tensile strain. If the $E = -3\,\mathrm{kV/cm}$ is removed, the in-plane strain returns to the ***O*** state. Accordingly, the resistance of the film recovers to the initial value (***O′*** state).

Using this ferroelastic strain effect, memory-type reversible resistance switching can be realized by applying appropriate electric field pulses to the LCMO/PINT structure, as shown in Fig. 13(c). Upon applying a sequence of $E = \pm 3\,\mathrm{kV/cm}$ pulses across the PINT to switch the polarization direction between the in-plane and downward directions, corresponding binary ***O*** and ***B*** resistance states can be generated. The reversible resistance modulation at room temperature reaches ~5%, which is comparable to other reports when using PMNT(011) substrates [18,25]. Compared with electrical-current-driven electronic devices, this dynamic electric-field-impulse-induced nonvolatile memory-type resistance switching may have applications for low energy consumption, nonvolatile memory devices due to the electric field impulse control of the resistance with extremely small current (nanoamperes) in the substrate.

If the temperature of the LCMO/PINT sample is lowered to 260 K, a larger electric field is needed to cycle a sufficiently large resistance-electric field hysteresis loop ($\boldsymbol{O} \rightarrow \boldsymbol{A} \rightarrow \boldsymbol{B} \rightarrow \boldsymbol{C} \rightarrow \boldsymbol{O}$) [inset of Fig. 14(a)], due to the increase in the coercive field of the PINT at low temperatures. The two reversible resistance states, ***O*** and ***B***, represent two stable remnant strain states with out-of-plane (P_r^-) and in-plane ($P_r^{\parallel}$) polarization directions, respectively, as schematically shown in Figs. 14(c) and 14(d), respectively. *In situ* XRD measurements showed that both the PINT (111) and LCMO (111) diffraction peaks shift to higher 2θ angles upon switching the polarization direction from the P_r^- state to the $P_r^{\parallel}$ state [Figs. 14(e) and 14(f)], suggesting that the in-plane lattice (out-of-plane lattice) of both the PINT substrate and the LCMO film expands (contracts). Again, taking advantage of the ferroelastic strain, we achieved electric-field-controlled nonvolatile resistance switching by 16.7% at $T = 260\,\mathrm{K}$ [Fig. 14(b)]. This value is somewhat larger (~3.3 times) than that at room temperature. It is speculated that the

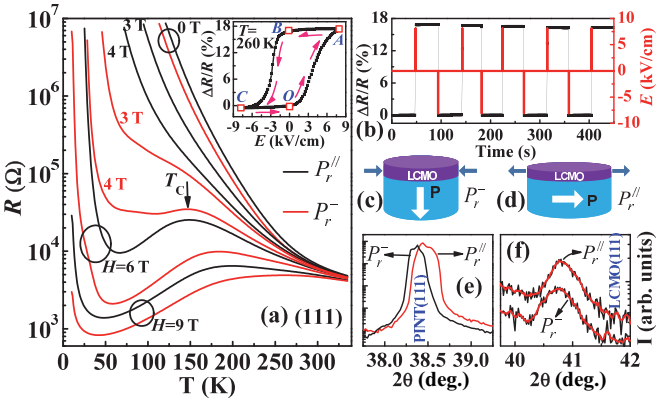

FIG. 14. (Color online) (a) Temperature dependence of resistance for the LCMO(111) film in the magnetic fields as stated when the PINT(111) substrate was in the $P_r^{\parallel}$ and P_r^- states, respectively. Inset in (a): $\Delta R/R$ of the film as a function of E at $T = 260\,\mathrm{K}$. (b) Nonvolatile resistance switching of the LCMO(111) film by a pulse electric field at $T = 260\,\mathrm{K}$. (c) and (d) Schematic diagrams for the ferroelastic strain effect at $T = 260\,\mathrm{K}$. (e) and (f) XRD θ–2θ scans for the PINT(111) substrate and LCMO(111) film when the PINT substrate was in the $P_r^{\parallel}$ and P_r^- states, respectively.

pronounced ferroelastic strain effect is also strongly associated with the electronic phase separation. With this motivation, we measured the temperature dependence of the resistance for the LCMO(111) film in magnetic fields up to 9 T for the P_r^- and $P_r^{\parallel}$ states and display the results in Fig. 14(a). For the P_r^- state and $H = 4\,\mathrm{T}$, upon decreasing temperature, the film underwent an insulator-to-metal phase transition at $T_C = 146\,\mathrm{K}$, and then reentered into the charge-ordered insulating state with $T_{\mathrm{CO}} \sim 108\,\mathrm{K}$. With increasing H, T_C was raised, while T_{CO} was suppressed. After the polarization was switched from the downward direction (i.e., the P_r^- state) towards the in-plane direction (i.e., the $P_r^{\parallel}$ state) [corresponding to an increase in the in-plane tensile strain of the film by approximately 0.1% using the XRD data shown in Fig. 14(f) and Poisson's ratio $\nu = 0.35$], the CO/AFI phase was significantly stabilized, as manifested by the absence of the insulator-to-metal phase transition at $H = 4\,\mathrm{T}$ for the $P_r^{\parallel}$ state and the remarkable increase of T_{CO} from 108 K for the P_r^- state to 171 K for the $P_r^{\parallel}$ state, as well as the increase in the resistance by at least three orders of magnitude at $T = 60\,\mathrm{K}$ for $H = 4\,\mathrm{T}$. Such a significant ferroelastic strain-induced stabilization of the CO/AFI phase is unprecedented for similar manganite film/FE structures.

Finally, we show in Fig. 15 the temperature dependence of MR for the LCMO(111) film at various magnetic fields for the P_r^- and $P_r^{\parallel}$ states. In sharp contrast to the FE poling-induced enhancement of the MR effect [see Figs. 6(a) and 6(b)], the ferroelastic domain switching-induced in-plane tensile strain suppresses MR over the entire temperature range; e.g., for $H = 3\,\mathrm{T}$, MR is reduced by 12.5% at $T = 120\,\mathrm{K}$ associated with the switching of the polarization from the P_r^- state to the $P_r^{\parallel}$ state. A noteworthy feature is that with increasing H, the effects of ferroelastic domain switching-induced in-plane tensile strain on MR effect are progressively suppressed. Particularly, at $H = 9\,\mathrm{T}$, the ferroelastic strain almost has no

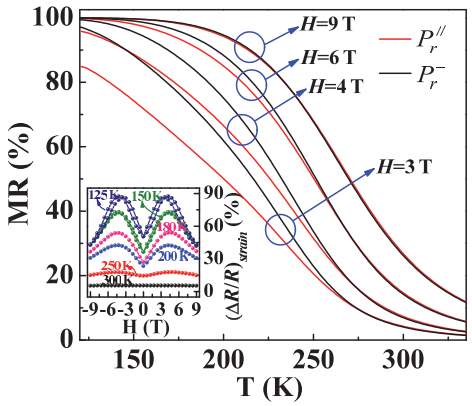

FIG. 15. (Color online) Temperature dependence of MR in the magnetic fields as stated for the LCMO(111) film when the PINT(111) substrate was in the $P_r^{\parallel}$ and P_r^{-} state, respectively. Inset shows $(\Delta R/R)_{\text{strain}}$ versus H curves for the film at the temperatures stated.

impact on the MR, as reflected by the similar MR versus T curves for the P_r^{-} and $P_r^{\parallel}$ states. Based on the transport data shown in Fig. 4(b) and Fig. 14(a), it is concluded that whether the FE substrate-induced strain is compressive or tensile, a high magnetic field tends to suppress the strain effect because the CO/AFI phase would be almost completely melted and converted to the FMM phase in a high magnetic field. Namely, the volume fraction of the FMM phase would be saturated at $H = 9\,\text{T}$. Under such circumstance, the application of a compressive or tensile strain to the film contributes little to the MR since there remains almost no CO/AFI phase that could be converted to the FMM phase by the strain. This effect of ferroelastic strain on MR further demonstrates that the interaction of the magnetic field with the strain is strongly associated with the electronic phase separation. We further evaluated the ferroelastic strain effect against magnetic field by measuring $(\Delta R/R)_{\text{strain}}$ as a function of H and illustrated the results in the inset of Fig. 15. The maximum $(\Delta R/R)_{\text{strain}}$ appears at $H \sim 4.2\,\text{T}$, suggesting the strongest electronic phase separation occurs at $H = 4.2\,\text{T}$, where the ferroelastic domain switching-induced tensile strain could easily convert the FMM phase to the CO/AFI phase, thereby causing an increase in resistance up to ~87.4% at $T = 125\,\text{K}$, resulting in a gauge factor $(\Delta R/R)_{\text{strain}}/\varepsilon_{xx(\text{film})} \sim 87{,}400\%$ and thus demonstrating extreme sensitivity of the electronic phase separation to the strain. Similarly, at $T = 180\,\text{K}$, the film shows the maximum electronic phase separation at $H = 4.8\,\text{T}$, as reflected by the largest $(\Delta R/R)_{\text{strain}} \sim 53.9\%$ at $H = 4.8\,\text{T}$. These magnetic-field-tunable ferroelastic strain effects reveal that the electronic phase separation is the crucial ingredient that is responsible for the mutual interactions between the ferroelastic strain and the magnetic field and demonstrate the effectiveness of electric-field-controlled strain-tunability of the electronic phase separation.

IV. CONCLUSIONS

In summary, we have reported a comprehensive study of *in situ* FE/ferroelastic domain switching-induced strain on magnetotransport and magnetic properties as well as the electronic phase separation of half-doped LCMO thin films epitaxially grown on PMNT and PINT substrates. The substrate-poling-induced in-plane compressive strain causes a considerable increase in the magnetization and MR as well as a decrease in T_{CO} and resistance, resulting in a tremendous strain-tunability of resistance $(\Delta R/R)_{\text{strain}}/\varepsilon_{xx(\text{film})} \sim 220\,800\%$. Such a strain effect was found to be magnetically tunable. This, together with the strain-tunable MR effect, demonstrates strong mutual coupling between the strain and the magnetic field, which is essentially mediated by the electronic phase separation. Further studies show that the relative strength of the electronic phase separation could be monitored by measuring $(\Delta R/R)_{\text{strain}}$ against magnetic field and temperature. In sharp contrast, the ferroelastic domain switching-induced in-plane tensile strain leads to an increase in the resistance and T_{CO} and a drop in MR, signaling the stabilizing of the charge-ordered phase. Further, taking advantage of 180° FE domain switching, we clearly demonstrate that it is the interface strain coupling, and not the interface electric charge, that dominates the electronic transport and magnetic properties of LCMO films. Additionally, we achieved electric-field control of resistance using the electric-field-induced rhombohedral-to-tetragonal structural phase transition and realized electric-field-impulse-induced nonvolatile resistance modulation at room temperature using the reversible ferroelastic domain switching.

ACKNOWLEDGMENTS

This paper was supported by the National Science Foundation of China (Grants No. 51172259, No. 51428202, No. 51332007, and No. 11090332), the National Basic Research Program of China (Grants No. 2012CB922003 and No. 2015CB921201), the CAS/SAFEA International Partnership Program for Creative Research Teams, and the Fundamental Research Funds for the Central Universities (Grant No. WK2340000052).

[1] S. Mori, C. H. Chen, and S.-W. Cheong, Nature **392**, 473 (1998).
[2] A. Moreo, S. Yunoki, and E. Dagotto, Science **283**, 2034 (1999).
[3] P. G. Radaelli, D. E. Cox, M. Marezio, S.-W. Cheong, P. E. Schiffer, and A. P. Ramirez, Phys. Rev. Lett. **75**, 4488 (1995).
[4] G. H. Aydogdu, Y. Kuru, and H.-U. Habermeier, J. Cryst. Growth **310**, 4521 (2008).
[5] G. H. Aydogdu, Y. Kuru, and H.-U. Habermeier, Mater. Sci. Eng. B **144**, 123 (2007).
[6] D. Gutiérrez, G. Radaelli, F. Sánchez, R. Bertacco, and J. Fontcuberta, Phys. Rev. B **89**, 075107 (2014).
[7] V. G. Prokhorov, V. A. Komashko, G. G. Kaminsky, Y. P. Lee, S. Y. Park, Y. H. Hyun, V. L. Svetchnikov, K. W. Kim, and J. Y. Rhee, Low Temp. Phys. **32**, 128 (2006).
[8] Z.-H. Wang, O. I. Lebedev, G. Van Tendeloo, G. Cristiani, and H.-U. Habermeier, Phys. Rev. B **77**, 115330 (2008).

[9] S. Cox, J. C. Loudon, A. J. Williams, J. P. Attfield, J. Singleton, P. A. Midgley, and N. D. Mathur, Phys. Rev. B **78**, 035129 (2008).

[10] Y. M. Xiong, G. Y. Wang, X. G. Luo, C. H. Wang, X. H. Chen, X. Chen, and C. L. Chen, J. Appl. Phys. **97**, 083909 (2005).

[11] Y. G. Zhao, W. Cai, J. Zhao, X. P. Zhang, B. S. Cao, M. H. Zhu, L. W. Zhang, S. B. Ogale, T. Wu, T. Venkatesan, L. Lu, T. K. Mandal, and J. Gopalakrishnan, Phys. Rev. B **65**, 144406 (2002).

[12] I. O. Troyanchuk, D. D. Khalyavin, S. V. Trukhanov, and G. N. Chobot, and H. Szymczak, JETP Lett. **70**, 590 (1999).

[13] *Colossal Magnetoresistive Oxides*, edited byY. Tokura (Gordon & Breach, Tokyo, 1999).

[14] A. D. Rata, A. Herklotz, K. Nenkov, L. Schultz, and K. Dörr, Phys. Rev. Lett. **100**, 076401 (2008).

[15] A. Herklotz, A. D. Rata, L. Schultz, and K. Dörr, Phys. Rev. B **79**, 092409 (2009).

[16] M. C. Dekker, A. Herklotz, L. Schultz, M. Reibold, K. Vogel, M. D. Biegalski, H. M. Christen, and K. Dörr, Phys. Rev. B **84**, 054463 (2011).

[17] T. Jiang, S. W. Yang, Y. K. Liu, Y. W. Yin, S. N. Dong, W. B. Zhao, and X. G. Li, Appl. Phys. Lett. **103**, 053504 (2013).

[18] Y. J. Yang, Z. L. Luo, M. M. Yang, H. L. Huang, H. B. Wang, J. Bao, G. Q. Pan, C. Gao, Q. Hao, S. T. Wang, M. Jokubaitis, W. Z. Zhang, G. Xiao, Y. P. Yao, Y. K. Liu, and X. G. Li, Appl. Phys. Lett. **102**, 033501 (2013).

[19] J. Wang, F. X. Hu, L. Chen, Y. Y. Zhao, H. X. Lu, J. R. Sun, and B. G. Shen, Appl. Phys. Lett. **102**, 022423 (2013).

[20] J. F. Wang, Y. C. Jiang, Z. P. Wu, and J. Gao, Appl. Phys. Lett. **102**, 071913 (2013).

[21] R. K. Zheng, Y. Wang, J. Wang, K. S. Wong, H. L. W. Chan, C. L. Choy, and H. S. Luo, Phys. Rev. B **74**, 094427 (2006).

[22] Q. P. Chen, J. J. Yang, Y. G. Zhao, S. Zhang, J. W. Wang, M. H. Zhu, Y. Yu, X. Z. Zhang, Z. Wang, B. Yang, D. Xie, and T. L. Ren, Appl. Phys. Lett. **98**, 172507 (2011).

[23] E. J. Guo, J. Gao, and H. B. Lu, Appl. Phys. Lett. **98**, 081903 (2011).

[24] B. W. Zhi, G. Y. Gao, H. R. Xu, F. Chen, X. L. Tan, P. F. Chen, L. F. Wang, and W. B. Wu, ACS Appl. Mater. Interf. **6**, 4603 (2014).

[25] M. Liu, J. Hoffman, J. Wang, J. X. Zhang, B. Nelson-Cheeseman, and A. Bhattacharya, Sci. Rep. **3**, 1876 (2013).

[26] J.-Y. Kim, L. D. Yao, and S. van Dijken, J. Phys.: Condens. Matter **25**, 082205 (2013).

[27] H. Ding, J. W. Cheah, L. Chen, T. Sritharan, and J. L. Wang, Thin Solid Films **522**, 420 (2012).

[28] Z. G. Wang, Y. Zhang, R. Viswan, Y. X. Li, H. S. Luo, J. F. Li, and D. Viehland, Phys. Rev. B **89**, 035118 (2014).

[29] M. M. Yang, X. Q. Zhao, J. Wang, Q. X. Zhu, J. X. Zhang, X. M. Li, H. S. Luo, X. G. Li, and R. K. Zheng, Appl. Phys. Lett. **104**, 052902 (2014).

[30] E. J. Guo, K. Dorr, and A. Herklotz, Appl. Phys. Lett. **101**, 242908 (2012).

[31] D. Dale, A. Fleet, J. D. Brock, and Y. Suzuki, Appl. Phys. Lett. **82**, 3725 (2003).

[32] W. Eerenstein, M. Wiora, J. L. Prieto, J. F. Scott, and N. D. Mathur, Nat. Mater. **6**, 348 (2007).

[33] X. Moya, L. E. Hueso, F. Maccherozzi, A. I. Tovstolytkin, D. I. Podyalovskii, C. Ducati, L. C. Phillips, M. Ghidinil, O. Hovorka, A. Berger, M. E. Vickers, E. Defay, S. S. Dhesi, and N. D. Mathur, Nat. Mater. **12**, 52 (2013).

[34] G. E. Sterbinsky, B. W. Wessels, J.-W. Kim, E. Karapetrova, P. J. Ryan, and D. J. Keavney, Appl. Phys. Lett. **96**, 092510 (2010).

[35] S. Geprägs, D. Mannix, M. Opel, S. T. B. Goennenwein, and R. Gross, Phys. Rev. B **88**, 054412 (2013).

[36] H. S. Luo, G. S. Xu, H. Q. Xu, P. C. Wang, and Z. W. Yin, Jpn. J. Appl. Phys., Part 1 **39**, 5581 (2000).

[37] Y. Y. Zhang, X. B. Li, D. A. Liu, Q. H. Zhang, W. Wang, B. R. D. Lin, X. Y. Zhao, and H. S. Luo, J. Cryst. Growth **318**, 890 (2011).

[38] See Supplemental Material at http://link.aps.org/supplemental/10.1103/PhysRevB.90.224420 for Figs. S1, S2, and S3.

[39] E. D. Specht, H. M. Christen, D. P. Norton, and L. A. Boatner, Phys. Rev. Lett. **80**, 4317 (1998).

[40] S. P. Timoshenko and J. N. Goodier, *Theory of Elasticity* (McGraw-Hill, New York, 1987), Chap. 2.

[41] C. Adamo, X. Ke, H. Q. Wang, H. L. Xin, T. Heeg, M. E. Hawley, W. Zander, J. Schubert, P. Schiffer, D. A. Muller, L. Maritato, and D. G. Schlom, Appl. Phys. Lett. **95**, 112504 (2009).

[42] D. Fuchs, E. Arac, C. Pinta, S. Schuppler, R. Schneider, and H. v. Löhneysen, Phys. Rev. B **77**, 014434 (2008).

[43] C. Thiele, K. Dörr, S. Fähler, L. Schultz, D. C. Meyer, A. A. Levin, and P. Paufler, Appl. Phys. Lett. **87**, 262502 (2005).

[44] R. K. Zheng, H.-U. Habermeier, H. L. W. Chan, C. L. Choy, and H. S. Luo, Phys. Rev. B **80**, 104433 (2009).

[45] H. J. A. Molegraaf, J. Hoffman, C. A. F. Vaz, S. Gariglio, D. van der Marel, C. H. Ahn, and J.-M. Triscone, Adv. Mater. **21**, 3470 (2009).

[46] L. H. Liu, X. Wu, S. Wang, W. N. Di, D. Lin, X. Y. Zhao, and H. S. Luo, J. Cryst. Growth. **318**, 856 (2011).

[47] A. Herklotz, J. D. Plumhof, A. Rastelli, O. G. Schmidt, L. Schultz, and K. Dörr, J. Appl. Phys. **108**, 094101 (2010).

[48] X. Zhao, J. Wang, Z. Peng, H. L. W. Chan, H. Luo, and C. L. Choy, Phys. Status Solidi A **198**, R1 (2003).

[49] T. Wu, A. Bur, P. Zhao, K. P. Mohanchandra, K. Wong, K. L. Wang, C. S. Lynch, and G. P. Carman, Appl. Phys. Lett. **98**, 012504 (2011).

[50] S. Zhang, Y. G. Zhao, X. Xiao, Y. Z. Wu, S. Rizwan, L. F. Yang, P. S. Li, J. W. Wang, M. H. Zhu, H. Y. Zhang, X. F. Jin, and X. F. Han, Sci. Rep. **4**, 3727 (2014).

[51] Y.-H. Chu, L. W. Martin, M. B. Holcomb, M. Gajek, S.-J. Han, Q. He, N. Balke, C.-H. Yang, D. Lee, W. Hu, Q. Zhan, P.-L. Yang, A. Fraile-Rodríguez, A. Scholl, S. X. Wang, and R. Ramesh, Nat. Mater. **7**, 478 (2008).

[52] M. Trassin, J. D. Clarkson, S. R. Bowden, J. Liu, J. T. Heron, R. J. Paull, E. Arenholz, D. T. Pierce, and J. Unguris, Phys. Rev. B **87**, 134426 (2013).

[53] C. A. F. Vaz, J. Hoffman, Y. Segal, J. W. Reiner, R. D. Grober, Z. Zhang, C. H. Ahn, and F. J. Walker, Phys. Rev. Lett. **104**, 127202 (2010).

[54] T. Kanki, Y.-G. Park, H. Tanaka, and T. Kawai, Appl. Phys. Lett. **83**, 4860 (2003).

[55] T. Wu, P. Zhao, M. Bao, A. Bur, J. L. Hockel, K. Wong, K. P. Mohanchandra, C. S. Lynch, G. P. Carman, J. Appl. Phys. **109**, 124101 (2011).